
What You See is What You Classify: Black Box Attributions

Steven Stalder
Swiss Data Science Center
ETH Zurich, Switzerland

Nathanaël Perraudin
Swiss Data Science Center
ETH Zurich, Switzerland

Radhakrishna Achanta
Swiss Data Science Center
EPFL, Switzerland

Fernando Perez-Cruz
Swiss Data Science Center
ETH Zurich, Switzerland

Michele Volpi
Swiss Data Science Center
ETH Zurich, Switzerland

Abstract

An important step towards explaining deep image classifiers lies in the identification of image regions that contribute to individual class scores in the model’s output. However, doing this accurately is a difficult task due to the black-box nature of such networks. Most existing approaches find such attributions either using activations and gradients or by repeatedly perturbing the input. We instead address this challenge by training a second deep network, the *Explainer*, to predict attributions for a pre-trained black-box classifier, the *Explanandum*. These attributions are in the form of masks that only show the classifier-relevant parts of an image, masking out the rest. Our approach produces sharper and more boundary-precise masks when compared to the saliency maps generated by other methods. Moreover, unlike most existing approaches, ours is capable of directly generating very distinct class-specific masks. Finally, the proposed method is very efficient for inference since it only takes a single forward pass through the *Explainer* to generate all class-specific masks. We show that our attributions are superior to established methods both visually and quantitatively, by evaluating them on the PASCAL VOC-2007 and Microsoft COCO-2014 datasets.

1 Introduction

Image recognition and classification systems based on deep learning are considered black boxes. It is often hard, if not impossible, to directly locate the portions of the input image responsible for a given classification output. Being able to systematically perform such attributions is a crucial step towards explainable deep learning, which can contribute to its widespread adoption. Attribution allows understanding the potential errors and biases [13, 17, 21]. It also enables the use of deep networks as decision support tools, *e.g.* in medicine [15], and facilitating meeting legal regulations [8]. Note that we refer to attribution as the goal of associating input image regions to model decisions, which differs from the notion of interpretability that relates to models that can be directly used to infer causal or general structural relationships that link inputs and outputs [23].

The problem of performing attribution for deep image classifiers has been addressed by several recent works. These belong to two broad categories. The first relies on visualising the derived model’s activations and backpropagated signals [31, 24, 3]. Although these methods provide a direct way to visualize salient areas, they heavily depend on the quality of the trained models’ architectures and weights. Furthermore, some of these methods turn out to be independent of the labels the model has been trained on, as well as to some extent the parameters of the models, as shown through randomization tests [1]. This suggests that many of these methods are strongly influenced

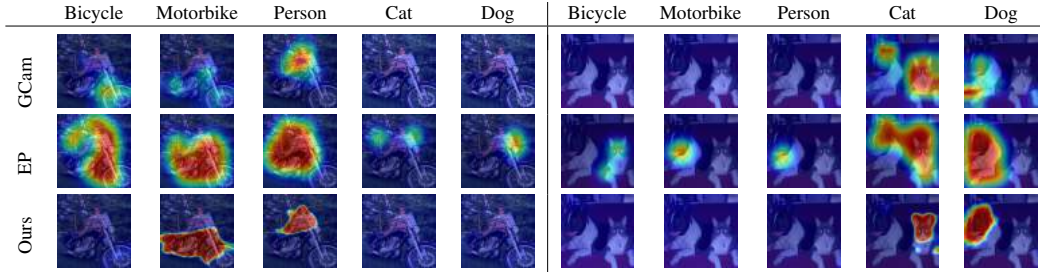


Figure 1: **Visual comparison of *per-class* attributions** provided for VOC-2007 by our *Explainer*, alongside Grad-CAM (GCam) [24] and Extremal Perturbations (EP) [12] for the VGG-16 architecture [25]. Our attributions have sharper boundaries and at the same time are more class-accurate than Grad-CAM or EP. Attributions for only five out of the twenty VOC-2007 classes are shown for convenience. Colormap ranges from low (blue) to high (red) saliency.

by low-level, class-agnostic features and are therefore inadequate. The second category relies on local perturbations of the input images and is often model-agnostic. These models rely on masking strategies to infer local feature importance, which often results in loss of visual detail, ambiguity and high computational cost. Nonetheless, results suggest that local perturbations, like masking, are an effective way to analyze and explain the response of a model [20, 22].

This last line of reasoning posits that attribution can be seen as a task independent of the *Explanandum* (*i.e.* the model to be explained). Therefore, it is natural to consider learning an *Explainer* (*i.e.* the model that explains) that specifically addresses the task of attribution. We approach attribution as a supervised meta-learning problem through the use of a complementary convolutional neural network, which learns to produce dense class-specific attribution masks, balancing preservation and deletion of information from the input image as dictated by the *Explanandum*.

The resulting *Explainer* efficiently masks and precisely locates regions of the input image that are responsible for the classification result of a pre-trained and frozen *Explanandum* (see Fig. 1 and Sup. Mat. Sec. C). We evaluate our methodology on PASCAL Visual Object Classes (VOC-2007) [9] and Microsoft Common Objects in Context (COCO-2014) [18]. To sum up, we present an efficient attribution method, which has the following advantages:

- Our *Explainer* provides a precise mask for each class label as in Fig. 1.
- Our *Explainer* provides attributions for test images with a single very efficient forward pass, orders of magnitude more efficient as compared to other perturbation-based approaches.
- At inference time, our *Explainer* does not need to access the *Explanandum*.

2 Related Work

Activation and gradient-based methods. The methods in this category attempt to explain a trained model by leveraging its weights and its activations for a given image to be explained. Zhou et al. [31] initiated this line of research with Class Activation Mapping (CAM), where the authors built particular architectures around a notion of global average pooling and illustrated the intrinsic localization performed by a classification network. Grad-CAM [24] removed the dependency of CAM on specific architectures by reconstructing the input heatmap through a weighted average of gradients, rather than directly projecting back activations. Further extensions to this are Grad-CAM++ [3], which is CAM weighted by averaged second order gradients, Score-CAM [29], which is CAM weighted by layer-wise class activations, or Ablation-CAM [7], which is CAM weighted by neuron ablation. Other extensions aim to cope with the issues arising from the high sensitivity to noise and clipping effects of gradients [1].

Some methods directly engineer the backpropagation and network architectures in order to retrieve pixel-level saliency maps. One such example is the deconvolution approach of Zeiler and Fergus [30], where the authors propose to revert forward propagation (mapping activations to pixels instead of mapping pixels to activations) to visualize features and functions of intermediate layers. From this, Springenberg et al. [26] derived guided backpropagation. Although the focus of their work

was on developing an efficient fully convolutional neural network, they show how by combining traditional backpropagation and deconvolutions, one can retrieve salient regions of the input for a specific class. In another line of work, Wagner et al. [28] frame the problem as a defense against adversarial perturbations and tackle it by constraining and selectively pruning activations.

Local perturbations and local models. The idea behind these methods is that by perturbing the input to the trained network, one can retrieve an explanation signal by summarizing changes in the classification scores. RISE introduced a way of retrieving a saliency heatmap based on random perturbations of the input image [20] and recently, [27] extended a similar reasoning for object detection systems. The input image is randomly masked several times, changes in the model scores tracked, and aggregated by a weighted average. LIME proposes a similar setup, but instead uses random switches on unsupervised segmentation [22].

Fong and Vedaldi [11] extend these ideas by reformulating the attribution problem as a meta-learning task, where the optimal mask can be found by optimizing a score. Fong et al. [12] extend their previous work [11] through the definition of *extremal perturbations*, which are the family of transformations that maximally affect a classification score. They propose to use Gaussian blur to assess perturbations over a fixed set of mask areas. Dabkowski and Gal [5] rely on a similar intuition, and the *Explainer* is directly optimized based on meta-learning around the *Explanandum*. In these settings, the *Explainer* optimizes a loss which balances preservation of the classification score on the active parts of the image, while minimizing the score for areas that are not active. These works also make use of regularization to constrain the mask area and its smoothness. In a similar fashion, Chang et al. [2] learn a pixel-specific dropout as a Bernoulli distribution, which is used to retrieve a mask and evaluate extremal perturbations. Unlike Fong et al. [12], Chang et al. [2] return the parameters of the learned per-pixel Bernoulli distribution as the saliency mask. Recently, Khorram et al. [16] proposed iGOS++, which frames attribution as optimizing over a mask which optimally balances preservation of useful information and removal of unnecessary information, regularized by bilateral total variation.

In this paper, we propose a method which learns a dense perturbation, the attribution mask, over input images. Unlike existing approaches, we optimize to balance low multi-label binary cross entropy for the unmasked portion of the input image, and high entropy for areas of the image masked out by the *Explainer*. Compared to most perturbation-based methods, our *Explainer* can predict attribution masks for all classes (and not only the predicted class) in a single forward pass, thereby being orders of magnitude faster. In addition, we beat state-of-the-art on standard benchmarks.

3 Training the *Explainer*

In this section, we present our *Explainer* architecture, which is trained to detect image regions that a given pre-trained classifier, the *Explanandum*, relies on to infer semantic object classes. Training of our model does *not* require any pixel-wise annotations. It relies on the *Explanandum*'s training data (including labels) and model. This makes our technique generalizable to any *Explanandum* architecture through which we can back-propagate the classification loss.

As illustrated in Fig. 2, the *Explainer* sees an image and outputs a set of masks \mathbf{S} of the same resolution, containing one segmentation mask s_c for each class $c \in C$. The values of the class masks s_c are bounded in the range $[0, 1]$ through a sigmoid function $\sigma(t) = e^t / (1 + e^t)$, where t represents the predicted pixel-wise logits. Values of 1 or 0 in the mask result in the full preservation or deletion of the corresponding pixel value, respectively. Note that the sum of the class masks does not need to be equal to one.

Using the target label(s) for the input image, we split the class segmentation masks into two sets: one that consists of masks that correspond to any ground truth class appearing in the training image, while the other contains the remaining ones. We merge each set into a single mask by taking the pixel-wise maximum value for each pixel position. The target mask \mathbf{m} (obtained from the first set) serves to locate the regions corresponding to any of the label(s) contained in a given training image, while the non-target mask \mathbf{n} (obtained from the second set) allows us to gather false positive activations. Finally, the inverted mask $\tilde{\mathbf{m}} = 1 - \mathbf{m}$ is used to ensure that once the object of interest is removed, the *Explanandum* cannot address the task anymore. Note that during inference, the mask aggregation step is not needed and our *Explainer* provides one explanation mask for each class.

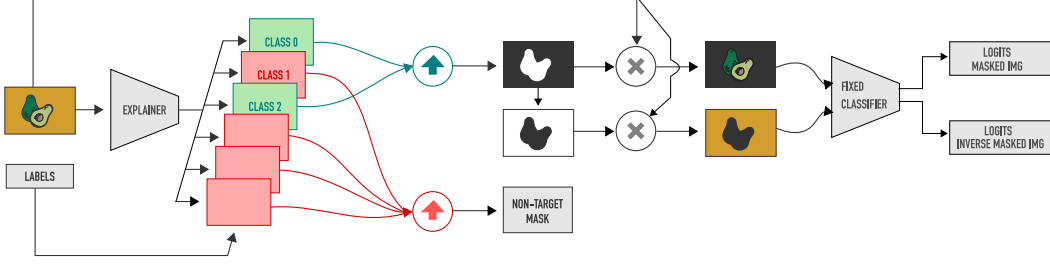


Figure 2: **Overview of our method.** Given a pre-trained classifier \mathcal{F} whose weights are frozen, the *Explainer* network \mathcal{E} learns to produce masks s_c for each class. The masks corresponding to the label(s) associated with the input image (shown in green) are merged by taking the pixel-wise maximum over masks (shown as \uparrow 's), to obtain a *target mask* \mathbf{m} and its complement $\tilde{\mathbf{m}}$ (*i.e.* inverted mask). All the other masks (shown in red), which do not correspond to the labels of the input image but might still score positively for the given image, are merged separately to obtain the *non-target mask* \mathbf{n} , which is also used in the loss term. The images obtained by multiplying the target mask and its complement with the input image (shown by \times 's) are fed to the given pre-trained classifier separately, generating two outputs on which we compute losses. The set of per-class masks \mathbf{S} and the aggregated *target mask* \mathbf{m} serve as the attributions provided by our *Explainer*.

3.1 Training loss

We formulate the loss as a combination of four terms, which reflect the desired conditions:

$$\mathcal{L}_E(\mathbf{x}, \mathcal{Y}, \mathbf{S}, \mathbf{m}, \mathbf{n}) = \mathcal{L}_c(\mathbf{x}, \mathcal{Y}, \mathbf{m}) + \lambda_e \mathcal{L}_e(\mathbf{x}, \tilde{\mathbf{m}}) + \lambda_a \mathcal{L}_a(\mathbf{m}, \mathbf{n}, \mathbf{S}) + \lambda_{tv} \mathcal{L}_{tv}(\mathbf{m}, \mathbf{n}), \quad (1)$$

where $\mathcal{L}_c(\mathbf{x}, \mathcal{Y}, \mathbf{m})$ is the binary cross-entropy loss over the masked image, $\mathcal{L}_e(\mathbf{x}, \tilde{\mathbf{m}})$ is an entropy term over the image masked with the complement of \mathbf{m} , $\mathcal{L}_a(\mathbf{m}, \mathbf{n}, \mathbf{S})$ is a regularization term accounting for the area of the true and false positive masks, and $\mathcal{L}_{tv}(\mathbf{m}, \mathbf{n})$ is a regularization term favouring smooth masks. λ_e , λ_a and λ_{tv} are hyperparameters balancing the loss terms.

Classification loss: $\mathcal{L}_c(\mathbf{x}, \mathcal{Y}, \mathbf{m})$. A model should be able to make correct decisions exclusively using the relevant portions of the image, ignoring all the rest. Under this assumption, we define the classification loss as a sum over binary cross-entropy terms, one for each class contained in the image.

Representing the *Explainer* as \mathcal{E} and the frozen *Explanandum* as \mathcal{F} , we define $\mathbf{p} = \mathcal{F}(\mathbf{x} \odot \mathbf{m})$ as the probability vector returned by the model \mathcal{F} applied on the masked image, using the aggregated (element-wise maximum) mask \mathbf{m} provided by \mathcal{E} . For all classes C in the training data and the set of target classes \mathcal{Y} in the image, we compute:

$$\mathcal{L}_c(\mathbf{x}, \mathcal{Y}, \mathbf{m}) = -\frac{1}{C} \sum_{c=1}^C [\![c \in \mathcal{Y}]\!] \log(\mathbf{p}[c]) + [\![c \notin \mathcal{Y}]\!] \log(1 - \mathbf{p}[c]), \quad (2)$$

where $\llbracket c \in \mathcal{Y} \rrbracket$ denotes the Iverson bracket, returning 1 if the condition is true (the image contains class c), 0 otherwise. This allows training a mask when multiple classes are present in the training image, as in multi-label classification problems, where multiple masks are active at the same time and some pixels are free not to belong to any mask (contrarily to using cross-entropy). Therefore, the model is free to learn dependencies and co-occurrences between different classes. This loss pushes the *Explainer* to learn masks approximating $\mathcal{F}(\mathbf{x} \odot \mathbf{m}) \approx \mathcal{F}(\mathbf{x})$, *i.e.* masked images are classified as correctly as possible in the eyes of the (pre-)trained *Explanandum*.

Negative entropy loss: $\mathcal{L}_e(\mathbf{x}, \tilde{\mathbf{m}})$. This part of the loss pushes the *Explainer* to provide masks whose complements do not contain any discriminative visual cue, *i.e.* parts of the image that the *Explanandum* could use to infer the correct class. In other words, the classifier scores on the mask complement should provide class probabilities $\tilde{\mathbf{p}} = \mathcal{F}(\mathbf{x} \odot \tilde{\mathbf{m}})$ as uniform as possible. To this end, we aim at minimizing the negative entropy of the predictions over the class memberships, as:

$$\mathcal{L}_e(\mathbf{x}, \tilde{\mathbf{m}}) = \frac{1}{C} \sum_{c=1}^C \tilde{\mathbf{p}}[c] \log \tilde{\mathbf{p}}[c] \quad (3)$$

Note that this loss is the negative entropy, as we aim for a high entropy for the background.

Area loss: $\mathcal{L}_a(\mathbf{m}, \mathbf{n}, \mathbf{S})$. With the terms \mathcal{L}_c and \mathcal{L}_e alone, our *Explainer* would have no incentive to produce a target mask that conceals image areas. Clearly, a target mask \mathbf{m} with 1 everywhere would minimize these terms with respect to \mathbf{m} . To make sure \mathbf{m} conceals background, we add two terms to the loss that correspond to two crucial desiderata: The mask should be as small as possible, but if the objective would favour larger areas, a whole range of areas in between a minimal and maximal percentage should not be penalized further.

The regularization over the area is simply formulated as the mean of the mask values, computed as $\mathcal{A}(\mathbf{m}) = \frac{1}{Z} \sum_{i,j} \mathbf{m}[i, j]$, where Z is the number of pixels. We want this area to be small, but non-zero. The same is required of the non-target mask \mathbf{n} as well.

The term bounding the mask area from both above and below is formulated starting from the constraint presented by Fong et al. [12]. However, instead of constraining the final image mask to a fixed area, we extend their technique to determine a valid minimum area a and a maximum area b for those class segmentation masks that correspond to at least one object in the image.

Given such a class segmentation mask s_c , we flatten it to a one-dimensional vector, and then sort its values in descending order. Let $v(s_c)$ be the vectorization operation and $r(v(s_c))$ be the sorting of the vectorized class mask s_c . We then define two vectors \mathbf{q}_{\min} and \mathbf{q}_{\max} , each starting with a predefined number of 1's and padded with 0's to match the length of $v(s_c)$, where the amount of 1 corresponds to the minimum $0 < a < b$ or maximum $a < b < 1$ area, respectively. We also define \mathbf{q}_{mask} , which corresponds to s_c , vectorized, and sorted. Concretely:

$$\mathbf{q}_{\text{mask}} = r(v(s_c)) \in [0, 1]^Z, \quad \mathbf{q}_{\min} = [\mathbf{1}^{\lfloor Za \rfloor} \dots \mathbf{0}^{\lfloor Z(1-a) \rfloor}], \quad \mathbf{q}_{\max} = [\mathbf{1}^{\lfloor Zb \rfloor} \dots \mathbf{0}^{\lfloor Z(1-b) \rfloor}]. \quad (4)$$

To constrain the minimum and maximum area covered by the class segmentation mask, we then compute an area bounding measure \mathcal{B} given by:

$$\mathcal{B}(\mathbf{s}) = \frac{1}{Z} \sum_i^Z \max(\mathbf{q}_{\min}[i] - \mathbf{q}_{\text{mask}}[i], 0) + \frac{1}{Z} \sum_i^Z \max(\mathbf{q}_{\text{mask}}[i] - \mathbf{q}_{\max}[i], 0). \quad (5)$$

where the first term penalizes the mask only if the largest $\lfloor Za \rfloor$ values are smaller than 1, while the second term penalizes the smallest $Z - \lfloor Zb \rfloor$ values greater than 0. Our goal is for the mask to cover *at least* a certain area independently of its maximum size.

The final area regularization is therefore:

$$\mathcal{L}_a(\mathbf{m}, \mathbf{n}, \mathbf{S}) = \mathcal{A}(\mathbf{m}) + \mathcal{A}(\mathbf{n}) + \frac{\sum_{c=1}^C \mathbb{1}[c \in \mathcal{Y}] \mathcal{B}(s_c)}{\sum_{c=1}^C \mathbb{1}[c \in \mathcal{Y}]} \quad (6)$$

where \mathcal{Y} is again the subset of the classes that are present in the given input image according to the given training labels. Note that the last term of (6) used in conjunction with the smoothness loss presented below favors masks with sharp transitions between 0 and 1.

Smoothness Loss: $\mathcal{L}_{tv}(\mathbf{m}, \mathbf{n})$. As a final requirement, we are interested in generating masks that appear smooth and free of artifacts. For this purpose, we utilize a total variation (TV) loss on the masks as used by Fong and Vedaldi [11] and Dabkowski and Gal [5], albeit we use the anisotropic variant given by:

$$\mathcal{TV}(\mathbf{x}) = \frac{1}{Z} \sum_{i,j} |\mathbf{x}[i, j] - \mathbf{x}[i+1, j]| + |\mathbf{x}[i, j] - \mathbf{x}[i, j+1]|. \quad (7)$$

where \mathbf{x} is a two-dimensional array of values. The smoothness term of the loss relates to the target mask \mathbf{m} and non-target mask \mathbf{n} as:

$$\mathcal{L}_{tv}(\mathbf{m}, \mathbf{n}) = \mathcal{TV}(\mathbf{m}) + \mathcal{TV}(\mathbf{n}) \quad (8)$$

This smoothness term encourages our attributions to appear visually coherent.

4 Experiments

We present three results to establish the advantages of our *Explainer* over existing approaches. Although continuous in nature, our masks show a sharp transition from background to foreground,

making it effectively binary. Additionally, our masks adhere tightly to region boundaries. Since common objective metrics may fail to convey this, we provide a brief visual comparison. The next result shows how our masks are class-specific, which provides more interpretive power than combined masks. The third result shows that our combined masks outperform existing methods on standard metrics for semantic segmentation.

Since we expect our *Explainer* to learn class-specific semantics and generate class-specific masks of the same resolution as the input image, we employ DeepLabV3 [4] with a ResNet-50 backbone, an architecture commonly used for semantic segmentation tasks. We train this model from scratch to avoid any bias, *i.e.* an information leakage from the semantic segmentation dataset from which DeepLabV3 has been pre-trained on.

For the *Explanandum*, we use VGG-16 [25] and ResNet-50 [14] models, both pretrained on ImageNet [6]. We fine-tune them on the multi-label classification tasks for VOC-2007 and COCO-2014, and then freeze the models. To this end, we use the full training set of VOC-2007 and 90% of the COCO-2014 training set for fine-tuning. To assess generalization, we use the test set of VOC-2007 and the validation set of COCO-2014, respectively. For choosing hyperparameters, we use the VOC-2007 validation set and the remaining 10% of the COCO-2014 training set. In this work, we implemented models and experiments using PyTorch [19] and PyTorch Lightning [10]¹.

4.1 Visual Comparison

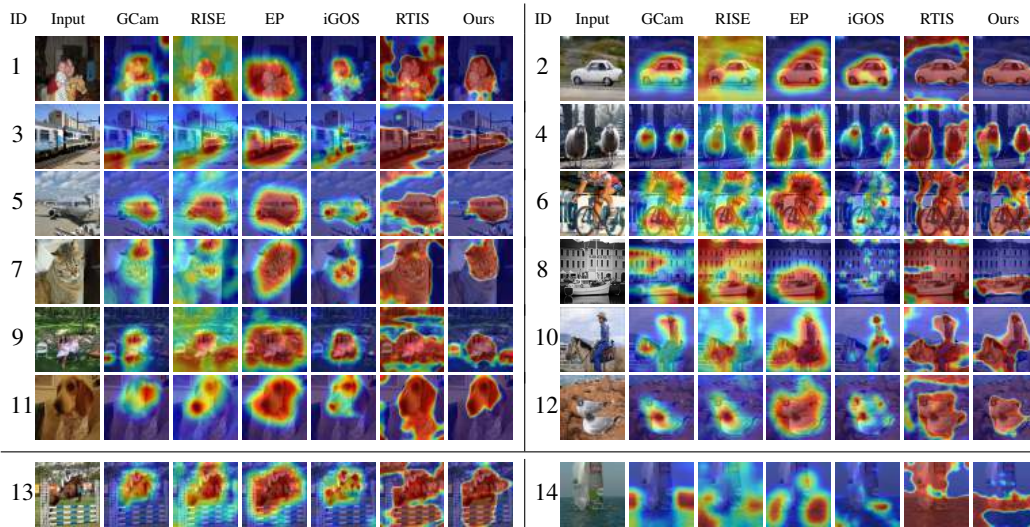


Figure 3: Visual comparison of our attributions for a VGG-16 network fine-tuned on images from the VOC-2007 dataset and frozen. Our attributions are much more effective at retaining object class regions and discarding the rest. Examples 13 and 14 show cases where our *Explainer* is inaccurate.

Visually, our *Explainer* leads to sharp and meaningful masks. Fig. 3 provides a visual comparison of how our *Explainer* attributions perform compared to the saliency maps obtained from Grad-CAM (GCam) [24], RISE [20], Extremal Perturbations (EP) [12], iGOS++ (iGOS) [16], and Real-Time Image Saliency (RTIS) [5]. For the RTIS baseline, we could not retrain their model on VOC-2007 and COCO-2014, as it was not possible to employ their architecture on multi-class classifiers. Instead, we use their loss to train our architecture. Accordingly, we fine-tuned some hyperparameters of our RTIS implementation, while leaving the remaining ones at the default values as given in their paper. For all our experiments, we resized input images to 224x224 pixels and normalized them on the mean and standard deviation of ImageNet.

Our approach provides sharp masks, which contrasts with classical saliency methods such as Grad-CAM or RISE. EP and iGOS++ provide masks which are better localized, although not as sharp as the ones produced by RTIS or our *Explainer*. Our implementation of RTIS provides sharp masks, but the overall attribution tends to be leaking over object borders. Our area constraints, in combination

¹Code is available at: <https://github.com/stevenstalder/NN-Explainer>

with the entropy term over the mask complement \tilde{m} , enforce tight masks over object classes of different sizes. For instance, Fig. 3(2), Fig. 3(5), or Fig. 3(8) show how our masks align much more clearly with the objects. This not only holds for single-class images, but also when we have multiple instances of the same class (Fig. 3(1), Fig. 3(4), Fig. 3(12)), or different classes (Fig. 3(6), Fig. 3(9), Fig. 3(10)). Attribution of some animals (*e.g.* Fig. 3(7), Fig. 3(10), Fig. 3(11)) often tends to be focusing on heads. Most training images containing animals have unobstructed heads, which can explain such behaviour. For some classes, all methods agree on the importance of an image region that is not actually part of the actual object. A good example for that is Fig. 3(3), where the train tracks are part of the attribution. Since most training images of trains also show train tracks, it seems obvious that the *Explanandum* learns to see the train tracks as discriminative semantic co-occurrence. With the help of an *Explainer*, such unintended biases can quickly be detected.

Fig. 3(13) and Fig. 3(14) show two examples where our *Explainer* is less precise. For Fig. 3(13), our attribution leaks over to the bars below the horse. Even though the classifier might indeed have made a connection between these bars and the “horse” class, Grad-CAM, RISE, EP, and iGOS++ appear to agree that the main importance should be attributed to the actual objects in the image. In Fig. 3(14), it is difficult to interpret our attribution for the class “boat” as some parts of the attribution lie on the actual object but also a significant area of the surrounding water is activated (underlining potential discriminative co-occurrence). However, the other methods also provide varying explanations, with iGOS++ masking mostly the boat, but Grad-CAM attributing all importance to the water. For more results on COCO-2014 and VOC-2007 please refer to Sup. Mat. Sec. D, E, and F.

4.2 Class-specific masking

<i>Explainer</i>		Mask					
		none	bottle	car	cat	dog	person
Target Class	bottle	20.57	15.29	4.91	4.82	4.82	2.72
	car	70.52	6.71	62.92	6.67	6.66	7.11
	cat	72.78	6.09	6.18	60.55	6.33	5.74
	dog	58.00	4.67	4.70	5.93	57.60	4.58
	person	69.37	8.90	6.18	5.83	6.57	71.01

<i>Grad-CAM</i>		Mask					
		none	bottle	car	cat	dog	person
Target Class	bottle	20.57	16.10	5.24	4.85	4.76	3.61
	car	70.52	6.93	50.19	6.65	6.53	8.92
	cat	72.78	6.17	6.39	43.74	8.99	5.85
	dog	58.00	4.46	4.39	8.23	41.88	4.38
	person	69.37	11.81	8.18	5.90	8.75	56.38

<i>RISE</i>		Mask					
		none	bottle	car	cat	dog	person
Target Class	bottle	20.57	18.67	10.94	12.05	10.70	9.73
	car	70.52	29.75	56.66	30.27	34.43	32.42
	cat	72.78	37.89	39.28	49.61	41.89	36.02
	dog	58.00	19.64	20.34	23.72	45.12	22.83
	person	69.37	56.06	53.39	47.33	54.81	63.52

<i>RTIS</i>		Mask					
		none	bottle	car	cat	dog	person
Target Class	bottle	20.57	18.92	11.19	13.37	13.44	17.24
	car	70.52	41.25	67.02	40.69	31.87	54.31
	cat	72.78	45.84	36.27	72.62	59.21	54.16
	dog	58.00	41.37	34.76	57.59	61.22	58.76
	person	69.37	64.71	54.41	43.42	61.55	73.59

Table 1: Comparison of class-specific masks generated by our *Explainer*, Grad-CAM [24], RISE [20], and adapted RTIS [5]. Images containing the target class specified in the row are masked with the thresholded class masks specified in the column and given to VGG-16 for classification. In any given cell we report the mean softmax probabilities over all mask thresholds and for every test image containing the target class. If the mask class equals the target class, we want high scores, if it is different, we want low scores. We additionally compute the softmax scores achieved for unmasked images (“none” column) for reference.

Our *Explainer* provides class-specific masks. In Fig. 1 we have already hinted at how our *Explainer* is able to provide more class-specific masks than the other techniques. In this section we evaluate this numerically. To this end, we have selected five target classes from the VOC-2007 dataset, for which we evaluate how the class masks interact with the classification confidence of the VGG-16 *Explanandum*. We have selected the classes “cat” and “dog” as they are two animals that often occur in similar settings, the most prevalent class “person” that can often be seen together with a variety of other classes and often inside the fourth class “car”, as well as the “bottle” class, to include a VOC-2007 class that is very difficult to detect for the *Explanandum*. For each test image containing one of the target classes, we first evaluate the classification performance of the *Explanandum* on the unmasked image (“none” column) and then on masked images where the image is masked once with each of the class-specific masks. Specifically, for each of these continuous masks we report the mean softmax probabilities for the target class, after we threshold each mask over nine uniform values in [0.1, 0.9] at 0.1 intervals. Note that here we use the softmax instead of the sigmoid function despite our multi-class setting since we want to evaluate the activation confidence for a single class compared

to all other (ideally masked-out) classes. This can of course affect the scores for the completely unmasked images where multiple object classes may be present.

In Tab. 1, we show the evaluations for our *Explainer*, Grad-CAM, RISE and RTIS. For EP and iGOS++, it was not feasible to conduct these experiments since these methods take a very long time to generate masks compared to the other ones (see Sup. Mat. Sec. A). We can clearly see how the masks produced by our method allow the *Explanandum* to retain very good classification confidence for the target classes when the correct mask is taken but render it completely uncertain when any other mask is put on the image. This is in stark contrast to RISE and RTIS especially, which produce overall larger, less precise masks. Even though the *Explanandum* has high confidence after masking the images with their corresponding correct masks, the same is still true when any wrong mask is used. Only Grad-CAM achieves comparable performance to our *Explainer* but results in considerably worse scores for the correct masks for 4 out of 5 classes and still shows some increased confidence when the wrong mask is put on the images of an often co-occurring target class (e.g. “cat” and “dog”, or “person” and “car”).

4.3 Segmentation accuracy

Data	Expl.	Metric	0	0.5	1	G.T.	GCam [24]	RISE [20]	EP [12]	iGOS++ [16]	RTIS [5]	Ours
VOC-2007	VGG	↑ Acc	66.29	50.00	33.71	100	70.53	56.98	63.91	70.17	59.63	74.60
		↑ IoU	0	23.42	33.71	100	28.78	28.62	34.95	24.05	39.94	38.04
		↓ Sal	-0.85	-0.53	0.15	-0.98	-1.41	-0.82	-0.77	-1.88	-0.31	-1.32
		↓ MAE	33.71	50.00	66.29	0	29.47	43.02	36.09	29.83	40.37	25.40
	ResNet	↑ Acc	66.29	50.00	33.71	100	68.54	57.37	61.43	69.23	50.77	73.56
		↑ IoU	0	23.42	33.71	100	30.75	28.42	34.88	24.25	36.46	34.23
		↓ Sal	-0.67	-0.68	-0.08	-1.13	-1.29	-1.02	-0.77	-1.92	-0.35	-1.33
		↓ MAE	33.71	50.00	66.29	0	31.46	42.63	38.57	30.77	49.23	26.44
COCO-2014	VGG	↑ Acc	70.39	50.00	29.61	100	66.31	52.35	57.01	68.70	39.18	69.90
		↑ IoU	0	20.87	29.61	100	25.63	25.50	29.23	20.35	31.16	31.59
		↓ Sal	-0.1	0.03	0.72	-0.38	-0.67	-0.31	-0.13	-1.12	0.65	-0.51
		↓ MAE	29.61	49.36	70.39	0	33.20	47.15	42.55	30.89	60.76	29.83
	ResNet	↑ Acc	70.39	50.00	29.61	100	67.25	55.05	56.92	69.57	41.40	65.30
		↑ IoU	0	20.87	29.61	100	24.84	25.98	29.75	21.63	30.76	27.42
		↓ Sal	0.2	-0.25	0.37	-0.88	-0.66	-0.44	-0.24	-1.19	0.17	-0.64
		↓ MAE	29.61	49.36	70.39	0	32.36	44.44	42.68	30.02	58.46	34.35

Table 2: Segmentation scores for the attribution models. We have compared the methods against the pixel-wise segmentation ground truths of all 210 VOC-2007 test images that include such annotations as well as for a randomly selected subset of 1000 COCO-2014 images out of our entire test set of over 41K images (due to long compute times of certain methods, see Sup. Mat. Sec. A). Columns “0”, “0.5”, “1” and “G.T.” (ground truth) represent the sanity check baselines to allow for a relative understanding of the scores. The upward arrows ↑ (downward arrows ↓) indicate that higher (lower) values are better.

Our attribution quality approaches object segmentation. While our *Explainer* architecture provides excellent attributions visually, we also confirm this quantitatively. Our explanations approximate object-level segmentation and can thus be evaluated using standard instance and semantic segmentation benchmarks. In Tab. 2 we illustrate the accuracy of the masking strategies, on VOC-2007 and COCO-2014, with VGG-16 and ResNet-50 as *Explanandum*, respectively. To provide a fair comparison with our method, we evaluate all methods by aggregating the masks from multiple classes into a single one, as shown in Fig. 3. We also provide four base measures that serve as sanity check baselines in Tab. 2), i.e. the columns “0”, “0.5”, “1”, and “G.T.” (ground truth). These measures show how the assessment metrics range under border conditions: with a completely null mask (composed of only 0’s), with a mask composed fully of 0.5’s, with a non-mask composed of only 1’s and finally with a mask which is perfectly equal to the ground truth segmentation.

We employ four different metrics, namely Accuracy (Acc), Mean IoU (IoU), Saliency (Sal) and Mean Absolute Error (MAE). All metrics are computed on a per-image basis, by using the ground truth segmentation masks and the aggregated mask of the true classes present in each image, then averaged over the test set. The Accuracy is computed pixel-wise over the continuous masks without

thresholding. The same holds for the IoU, where we take the pixel-wise minimum of the mask and the ground truth as the intersection and the maximum as the union, respectively. The Saliency score is adapted from Dabkowski and Gal [5], and computed as:

$$\text{Sal}(\mathbf{m}, p) = \log(\max(\mathcal{A}(\mathbf{m}), 0.05)) - \log\left(\sum_{c \in \mathcal{Y}} \mathbf{p}[c]\right), \quad (9)$$

where \mathcal{Y} is the set of classes present in the image. This metric balances the size of the mask \mathbf{m} with the *Explanandum* outputs. Smaller masks minimize the first term but have a tendency to lower the classification confidence, thus increasing the second term. It is therefore possible to get a lower score compared to the ground truth mask as a very small mask reduces the first term greatly, while it might still preserve a lot of the classification confidence. This is to the disadvantage of our method, as we aim to also attribute regions of lower (but still significant) importance instead of only the most distinguishing features. Finally, the MAE corresponds to the mean absolute error over the full dataset, which is computed for each input image as: $\text{MAE}(\mathbf{m}, \mathbf{g}) = \frac{1}{Z} \sum_{i,j} |\mathbf{m}[i, j] - \mathbf{g}[i, j]|$, where \mathbf{g} is the aggregated ground truth segmentation map for all object classes in the input image. Note that certain metrics might favor very small masks (*e.g.* Sal), while others favor very large masks (*e.g.* IoU).

The assessment in this sub-section assumes that an ideal method should perform attribution over the whole ground truth segmentation, which is not the case in certain situations, as attributions should only cover classifier-relevant parts of the object class (*e.g.* face instead of whole body). We argue that although attributions do not directly correspond to semantic segmentations, and while different methods target different goals for attribution, the combined evaluation of these metrics can still be used for a standardized assessment.

4.4 Limitations

Not all pairs of *Explainer* and *Explanandum* interact equally well and allow straightforward training. We observed that, while the explanation of VGG-16 and ResNet-50 on the VOC-2007 dataset performs consistently, the explanation for COCO-2014 is harder on ResNet-50 than on VGG-16 (see Sup. Mat. Sec. E and F), even though the accuracies are comparable (see Sup. Mat. Sec. B, Tab. 4). Sometimes, masks fail to precisely cover the discriminative objects parts. Some examples are given in Fig. 3(13) and Fig. 3(14), and further examples are given in the Sup. Mat. Sec. D, E and F.

5 Conclusions

We have presented an approach for visually attributing the classification result of a frozen, pre-trained, black-box classifier (the *Explanandum*) on specific regions of an input image. This involves training an *Explainer* architecture with the training data that was used to train the *Explanandum*. The resulting model generates attributions in the form of class-wise attribution masks, as well as an aggregated foreground mask with a single forward pass for any test image. As compared to the gradient and activation-based approaches, which often generate blurry saliency maps, our masks locate object regions more accurately and the delineation of these regions is sharp (Sec. 4.1). As compared to the approaches that use perturbed inputs, the *Explainer* is not only more precise, as we prove quantitatively (Sec. 4.2 and 4.3), but also computationally more efficient (Sup. Mat. Sec. A).

We observe that the *Explainer* can be learned well if the pre-trained classifier exhibits a good level of accuracy. Since learning the attribution fully depends on the signals provided by the *Explanandum*, this comes as no surprise. If instead of the original image, we use inputs that are masked by our *Explainer*, the accuracy may slightly decrease (Sup. Mat. Sec. B). Since our masks are so parsimonious in retaining the essential parts of the original image, it points to the fact that the drop in accuracy might come from the *Explanandum* being deprived of background-dependent biases. Therefore, once the *Explainer* is trained to generate masks, one could imagine retraining the *Explanandum* with the original as well as *Explainer*-masked data. This can ensure that classification accuracy can be both high and free of influences from non-object regions. Finally, while our work focuses on explaining deep image classifiers, we believe it should be possible to extend such an approach to other black box classifiers, other data modalities, and other learning tasks such as regression.

References

- [1] J. Adebayo, J. Gilmer, M. Muelly, I. Goodfellow, M. Hardt, and B. Kim. Sanity checks for saliency maps. In *Advances in Neural Information Processing Systems*, pages 9505–9515, 2018.
- [2] C.-H. Chang, E. Creager, and D. Goldenberg, A. an Duvenaud. Explaining image classifiers by counterfactual generation. In *International Conference on Learning Representations*, 2019.
- [3] A. Chattopadhyay, A. Sarkar, P. Howlader, and V. N. Balasubramanian. Grad-CAM++: Generalized gradient-based visual explanations for deep convolutional networks. In *IEEE Winter Conference on Applications of Computer Vision*, pages 839–847, 2018.
- [4] L.-C. Chen, G. Papandreou, F. Schroff, and H. Adam. Rethinking atrous convolution for semantic image segmentation. *arXiv preprint arXiv:1706.05587*, 2017.
- [5] P. Dabkowski and Y. Gal. Real time image saliency for black box classifiers. In *Advances in Neural Information Processing Systems*, pages 6967–6976, 2017.
- [6] J. Deng, W. Dong, R. Socher, L.-J. Li, K. Li, and L. Fei-Fei. ImageNet: A large-scale hierarchical image database. In *IEEE/CVF Conference on Computer Vision and Pattern Recognition*, pages 248–255. Ieee, 2009.
- [7] S. Desai and H. G. Ramaswamy. Ablation-CAM: Visual explanations for deep convolutional network via gradient-free localization. In *IEEE Winter Conference on Applications of Computer Vision*, pages 972–980, 2020.
- [8] F. Doshi-Velez, M. Kortz, R. Budish, C. Bavitz, S. Gershman, D. O’Brien, K. Scott, S. Schieber, J. Waldo, D. Weinberger, and et. al. Accountability of AI under the law: The role of explanation. *arXiv preprint arXiv:1711.01134*, 2017.
- [9] M. Everingham, S. M. A. Eslami, L. Van Gool, C. K. I. Williams, J. Winn, and A. Zisserman. The Pascal visual object classes challenge: A retrospective. *International Journal of Computer Vision*, 111(1):98–136, Jan. 2015.
- [10] W. Falcon et al. Pytorch lightning. *GitHub. Note: <https://github.com/PyTorchLightning/pytorch-lightning>*, 3:6, 2019.
- [11] R. C. Fong and A. Vedaldi. Interpretable explanations of black boxes by meaningful perturbation. In *IEEE International Conference on Computer Vision*, pages 3429–3437, 2017.
- [12] R. C. Fong, M. Patrick, and A. Vedaldi. Understanding deep networks via extremal perturbations and smooth masks. In *IEEE/CVF International Conference on Computer Vision*, pages 2950–2958, 2019.
- [13] L. H. Gilpin, D. Bau, B. Z. Yuan, A. Bajwa, M. Specter, and L. Kagal. Explaining explanations: An overview of interpretability of machine learning. In *IEEE International Conference on Data Science and Advanced Analytics*, pages 80–89, 2018.
- [14] K. He, X. Zhang, S. Ren, and J. Sun. Deep residual learning for image recognition. In *IEEE/CVF Conference on Computer Vision and Pattern Recognition*, pages 770–778, 2016.
- [15] A. Holzinger, C. Biemann, C. S. Pattichis, and D. B. Kell. What do we need to build explainable AI systems for the medical domain? *arXiv preprint arXiv:1712.09923*, 2017.
- [16] S. Khorram, T. Lawson, and L. Fuxin. iGOS++: Integrated gradient optimized saliency by bilateral perturbations. In *Proceedings of the Conference on Health, Inference, and Learning, CHIL ’21*, page 174–182, New York, NY, USA, 2021. Association for Computing Machinery. ISBN 9781450383592. doi: 10.1145/3450439.3451865. URL <https://doi.org/10.1145/3450439.3451865>.
- [17] Q. V. Liao, D. Gruen, and S. Miller. Questioning the AI: Informing design practices for explainable AI user experiences. In *Conference on Human Factors in Computing Systems*, 2020.
- [18] T.-Y. Lin, M. Maire, S. Belongie, J. Hays, P. Perona, D. Ramanan, P. Dollár, and C. L. Zitnick. Microsoft COCO: Common objects in context. In *European Conference on Computer Vision*, pages 740–755, 2014.
- [19] A. Paszke, S. Gross, S. Chintala, G. Chanan, E. Yang, Z. DeVito, Z. Lin, A. Desmaison, L. Antiga, and A. Lerer. Automatic differentiation in pytorch. 2017.
- [20] V. Petsiuk, A. Das, and K. Saenko. Rise: Randomized input sampling for explanation of black-box models. In *British Machine Vision Conference*, 2018.

- [21] G. Ras, N. Xie, M. van Gerven, and D. Doran. Explainable deep learning: A field guide for the uninitiated. *CoRR*, 2020.
- [22] M. T. Ribeiro, S. Singh, and C. Guestrin. "Why Should I Trust You?": Explaining the Predictions of Any Classifier. In *ACM SIGKDD International Conference on Knowledge Discovery and Data Mining*, pages 1135–1144, 2016.
- [23] C. Rudin. Stop explaining black box machine learning models for high stakes decisions and use interpretable models instead. *Nature Machine Intelligence*, 1:206–215, 2019.
- [24] R. R. Selvaraju, M. Cogswell, A. Das, R. Vedantam, D. Parikh, and D. Batra. Grad-CAM: Visual explanations from deep networks via gradient-based localization. In *IEEE/CVF International Conference on Computer Vision*, pages 618–626, 2017.
- [25] K. Simonyan and A. Zisserman. Very deep convolutional networks for large-scale image recognition. *arXiv preprint arXiv:1409.1556*, 2014.
- [26] J. T. Springenberg, A. Dosovitskiy, T. Brox, and M. Riedmiller. Striving for simplicity: The all convolutional net. In *International Conference on Learning Representations Workshops*, 2015.
- [27] V. Vitali Petsiuk, R. Jain, V. Manjunatha, V. I. Morariu, V. Mehra, V. Ordonez, and K. Saenko. Black-box explanation of object detectors via saliency maps. In *IEEE/CVF Computer Vision and Pattern Recognition*, 2021.
- [28] J. Wagner, J. M. Kohler, T. Gindele, L. Hetzel, J. T. Wiedemer, and S. Behnke. Interpretable and fine-grained visual explanations for convolutional neural networks. In *IEEE/CVF Conference on Computer Vision and Pattern Recognition*, pages 9097–9107, 2019.
- [29] H. Wang, Z. Wang, M. Du, F. Yang, Z. Zhang, S. Ding, P. Mardziel, and X. Hu. Score-CAM: Score-weighted visual explanations for convolutional neural networks. In *IEEE/CVF Conference on Computer Vision and Pattern Recognition Workshops*, pages 24–25, 2020.
- [30] M. D. Zeiler and R. Fergus. Visualizing and understanding convolutional networks. In *European Conference on Computer Vision*, pages 818–833, 2014.
- [31] B. Zhou, A. Khosla, A. Lapedriza, A. Oliva, and A. Torralba. Learning deep features for discriminative localization. In *IEEE/CVF Conference on Computer Vision and Pattern Recognition*, pages 2921–2929, 2016.

Supplementary Material

What You See is What You Classify: Black Box Attributions

A Compute Times

To evaluate the practicability of the methods, we have evaluated the time it takes for each method to generate all aggregated masks for the segmentation evaluation in Section 4.3. Note that this does not include any training time for our method and adapted RTIS (up to 12 hours on VOC-2007 and up to 2 days on COCO-2014), which only has to be performed once per model and dataset. Tab. 3 shows how significant the inference time differences between the methods are, even for a relatively small amount of images. RISE, EP and iGOS++ are orders of magnitude slower than GCAM, RTIS and our explainer. All experiments have been conducted using the same Tesla P100 PCIe 12GB GPU.

Dataset	Classifier	Method					
		GCAM	RISE	EP	iGOS++	RTIS	Explainer (ours)
VOC-2007	VGG-16	00:00:11	01:15:29	05:57:16	02:57:15	00:00:08	00:00:08
	Resnet-50	00:00:10	00:46:21	04:45:59	01:55:58	00:00:11	00:00:11
COCO-2014	VGG-16	00:01:23	06:00:47	33:54:33	28:55:22	00:00:34	00:00:34
	Resnet-50	00:01:30	03:41:35	26:40:42	19:09:10	00:00:47	00:00:47

Table 3: Time for computing segmentation masks with each method. The times are given in hh:mm:ss format. 210 and 1000 images have been segmented for VOC-2007 and COCO-2014, respectively.

B Classification accuracy

We demonstrate through Tab. 4 that our *Explainer* architecture does not adversely affect the performance of the (pre-)trained classification network. On occasions, a slight drop in accuracy can be expected, since each individual image changes quite drastically after being masked, not only visually, but also in terms of pixel intensity. Such drop can be simply explained by the fact that classifiers are not trained to recognize objects on a black background, which can behave as adversarial information to the VGG-16 and ResNet-50 classifiers. A loss in performance may also be indicative of the pre-trained classifier not being able to capitalize on an unexpected cue or correlations in the data (such as presence of blue and green in images with cows).

C Multiclass attribution examples on VOC using VGG-16 and ResNet-50

In this section, we show examples for the attribution over multiple classes on the VOC-2007 test set, using VGG-16 and ResNet-50 classifiers. In Fig. 4 and Fig. 5 below, each row corresponds to a random image from the VOC-2007 dataset, while each column corresponds to: the original image, the aggregated mask (per-pixel maximum over the class-masks), and the top 5 strongest attributed classes (TAC). Fig. 4 shows the results for VGG-16, while Fig. 5 shows the ones for ResNet-50. Each mask is scored according to the average mask activation (AMA), then sorted in descending order of the first 5 classes, as shown below. As this process is completely independent from the classifier itself, we also add the multi-label scores (logits through the sigmoid) for the original classifier on the unmasked image (CLS), multiplied by 100. When a class from the ground truth is attributed, the TAC is accompanied by two asterisks (**). We do not report the classification scores for the masked images, because they are greatly perturbed since the classifier has never learned to classify heavily masked images. For example, the classifier will give relatively high scores for all classes when it is given a completely black (all zeros) image.

Data	Model	Precision	Recall	F-Score
VOC-2007	VGG-16 Cl.	88.4	63.9	74.2
	VGG-16 Expl.	86.4	62.9	72.8
	ResNet-50 Cl.	85.2	72.3	78.2
	ResNet-50 Expl.	77.3	69.6	73.2
COCO-2014	VGG-16 Cl.	73.5	45.4	56.1
	VGG-16 Expl.	66.9	45.0	53.8
	ResNet-50 Cl.	77.6	44.6	56.6
	ResNet-50 Expl.	69.1	48.9	57.3

Table 4: Comparison between base (pre-trained, frozen) classifiers (Cl.) and their *explained* counterparts (Expl.) on the respective test sets. All numbers are given as percentages (%). Since masked images result in overall lower logits, we have used slightly different thresholds for the logits to count as positive versus negative predictions, depending on whether they result from unmasked or masked images. The presented numbers demonstrate that the use of our *Explainer* masks on the inputs to the pre-trained networks does not significantly affect their classification scores.

One can see that for both VGG-16 (Fig. 4) and ResNet-50 (Fig. 5), masks are sharp and outline (parts of) the object(s) of interest. By looking at the classification scores and the average mask activation, one can see that they usually correlate, meaning that the attribution works well. In those rare cases where the *Explainer* masks show their highest activation for classes that are not the ones for which the classifier gives the highest probability, the *Explainer* might have learned to detect those objects better than the classifier itself. Remember that those predictions are made directly on out-of-sample data. Also, note that the average mask activation does of course not directly relate to a classification, since smaller objects will give a smaller AMA score than large ones.

An interesting example is at the second row in Fig. 4, where in the fourth column (second most attributed class) the *Explainer* shows a significant attribution for class 5 (“bottle”) which is not present in the image. Only when looking at the classifier score on the unmasked image (CLS) this makes perfect sense since the classifier gives the “bottle” class a probability of over 60%. A similar example for this behavior is the fifth row in the same figure or the seventh row in Fig. 5. This indicates that the attributions by our *Explainer* are sensible even in failure cases of the classifier. In a few cases, the attributions for several classes are on the same image areas, as in the third and seventh rows of Fig. 5. This might happen for image areas that appear to be generally interesting for several classes at the same time but such cases are rare. In general, we see that ResNet-50 tends to provide masks with slightly more artifacts and spurious activations, when compared to the attributions of VGG-16.

Both experiments seem to agree that our *Explainer* is able to attribute classifiers to regions occupied by the correct class, or provide attributions caused by ambiguous biases in the classifier itself.

ID	Class name	ID	Class name
1	Aeroplane	2	Bicycle
3	Bird	4	Boat
5	Bottle	6	Bus
7	Car	8	Cat
9	Chair	10	Cow
11	Dining Table	12	Dog
13	Horse	14	Motorbike
15	Person	16	Potted Plant
17	Sheep	18	Sofa
19	Train	20	TV/Monitor

Table 5: Summary of the Pascal VOC-2007 Classes.


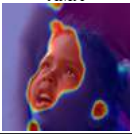
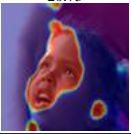

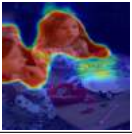
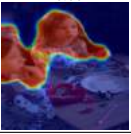

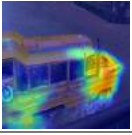
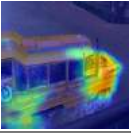




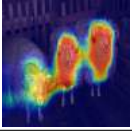
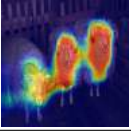





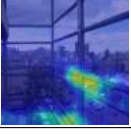

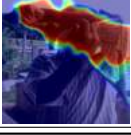
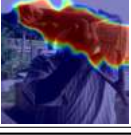
		1	2	3	4	5
	TAC	15 **	14	4	5	3
	CLS	98.44	1.76	1.52	4.07	0.96
	AMA	20.73	1.82	1.76	1.71	1.63
						
	TAC	15 **	5	11 **	3	13
	CLS	99.88	60.38	22.58	0.48	0.06
	AMA	26.06	9.87	4.49	2.10	2.06
						
	TAC	4 **	6	7	15	19
	CLS	5.94	73.04	1.37	7.15	1.32
	AMA	13.53	9.57	8.86	6.77	4.29
						
	TAC	7 **	15 **	17	10	18
	CLS	98.02	18.86	1.15	0.26	0.32
	AMA	21.86	4.02	2.18	1.81	1.60
						
	TAC	17 **	10	20	18	14
	CLS	50.11	15.73	0.00	0.02	0.01
	AMA	19.46	10.86	2.84	2.82	2.68
						
	TAC	15 **	5 **	14	4	17
	CLS	90.38	9.14	0.22	0.47	0.37
	AMA	18.27	12.87	1.48	1.41	1.41
						
	TAC	19	16 **	20	15	7 **
	CLS	13.01	11.27	1.33	8.28	15.31
	AMA	8.06	5.01	4.75	4.56	4.00
						
	TAC	15 **	3 **	13	18	14
	CLS	79.36	1.67	3.12	0.66	0.31
	AMA	26.72	2.74	2.52	2.35	2.14
						

Figure 4: Top-5 class-wise attributions for the VGG-16 classifier, for 8 random images from the VOC-2007 test set. Class-wise masks are sorted according to their average activation on the image plane. TAC corresponds to the top activating class, please refer to the legend in Tab. 5. CLS shows the respective class probabilities by the classifier on the original (unmasked) images, multiplied by 100. AMA shows the average mask activations for the respective class, also multiplied by 100.


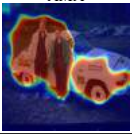
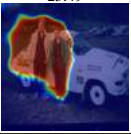
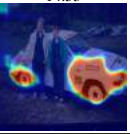




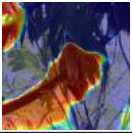
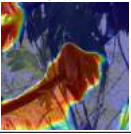




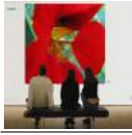
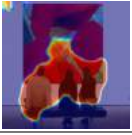
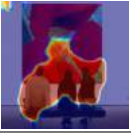





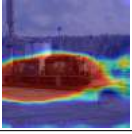
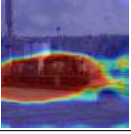





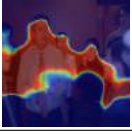
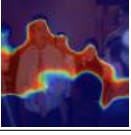












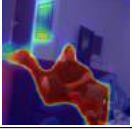
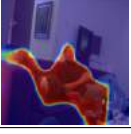
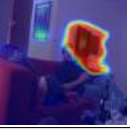






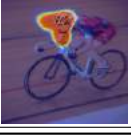

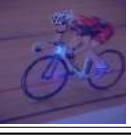
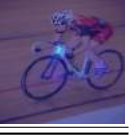
		1	2	3	4	5
	TAC	15 **	7 **	18	14	10
	CLS	77.13	52.68	0.56	1.19	0.96
	AMA	23.49	14.53	2.38	2.30	2.23
						
	TAC	3 **	2	9	17	11
	CLS	94.41	3.79	0.26	0.15	0.18
	AMA	32.71	0.52	0.47	0.46	0.45
						
	TAC	15 **	5	11	18	2
	CLS	96.07	1.26	2.08	28.53	0.76
	AMA	24.51	4.14	3.63	3.53	3.26
						
	TAC	19 **	17	9	10	11
	CLS	98.51	0.26	3.70	3.04	1.00
	AMA	30.16	0.89	0.86	0.86	0.83
						
	TAC	15 **	5	11	18	17
	CLS	99.95	12.24	35.63	2.34	0.15
	AMA	29.79	1.67	1.64	1.48	1.43
						
	TAC	7 **	14	13	9	10
	CLS	97.96	1.16	0.25	0.45	0.35
	AMA	31.01	0.55	0.54	0.52	0.48
						
	TAC	15 **	20	18 **	9	11
	CLS	76.80	33.23	90.83	66.43	4.12
	AMA	22.79	11.12	4.44	3.11	2.71
						
	TAC	2 **	15 **	9	11	4
	CLS	97.15	80.15	1.14	0.30	0.09
	AMA	13.52	5.68	1.64	1.49	1.36
						

Figure 5: Top-5 class-wise attributions for the ResNet-50 classifier, for 8 random images from the VOC-2007 test set. Class-wise masks are sorted according to their average activation on the image plane. TAC corresponds to the top activating class, please refer to the legend in Tab. 5. CLS shows the respective class probabilities by the classifier on the original (unmasked) images, multiplied by 100. AMA shows the average mask activations for the respective class, also multiplied by 100.

D Comparison of attribution methods on VOC-2007 using ResNet-50.

Figure 6 provides additional comparisons using ResNet-50 on VOC-2007. The comparison follows Fig. 3 of the manuscript. Overall, attribution methods for ResNet-50 are behaving better on VOC-2007 than on COCO-2014. Still, GCam, RISE and EP tend to provide smooth attributions, with the latter two sometimes scoring at multiple locations which are hard to relate to the classes present in the image. iGOS++ provides small activations that mostly seem to outline the most important object parts but sometimes also show artifacts that are difficult to interpret when it is less certain. RTIS provides masks that are often outlining objects, but fails in being sharp and providing clear attributions due to overshooting too much. Our *Explainer* method is mostly artifact-free and masks are very sharp on discriminative object parts.

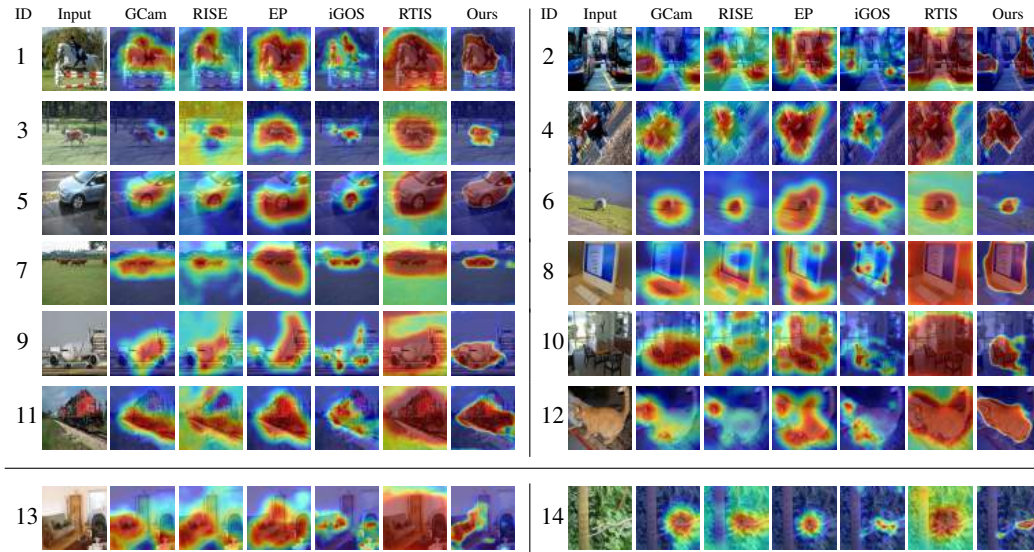


Figure 6: Comparison of attributions methods for a ResNet-50 network fine-tuned on images from the VOC-2007 dataset. Refer to Fig. 3 of the manuscript for more details.

E Comparison of attribution methods on COCO-2014 using VGG-16.

Figure 7 provides additional comparisons using VGG-16 on COCO-2014. The comparison follows Fig. 3 of the manuscript. Using VGG-16 on COCO-2014 results in good attributions, where masks are sharp and outline discriminative parts for the predicted classes precisely.

Not too differently than the results presented in the manuscript – attribution for the VGG-16 classifier on VOC-2007 – we can see that GCam [24] provides good attributions, if not for a fairly large smoothing. RISE [20] behaves similarly, and it often tends to provide several oversmoothed saliency locations, which are hard to interpret. EP [12] is much sharper, but also tends to overpredict attributions. On the other hand, iGOS++ shows small, localized attributions. However, it often also includes artifacts and sometimes does not capture certain objects at all. Finally, RTIS [5] does not show well delineated attribution on this combination of data and classifier as it overshoots too much to allow for a clear interpretation. Our *Explainer* provides localized attributions which are easy to interpret, with sharp boundaries, which in most cases coincide with the classes of interest or discriminative parts composing them. In general, the *Explainer* predicts compact masks with smaller areas, similarly to GCam, but much less smoothed overall.

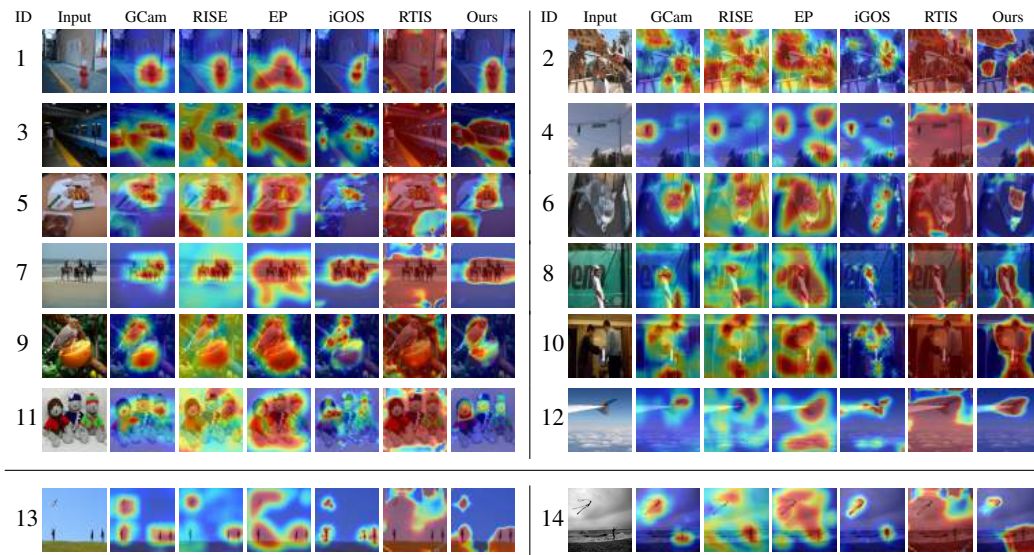


Figure 7: Comparison of attributions methods for a VGG-16 network fine-tuned on images from the COCO-2014 dataset. Refer to Fig. 3 of the manuscript for more details.

F Comparison of attribution methods on COCO-2014 using ResNet-50.

Figure 8 provides additional comparisons using ResNet-50 on COCO-2014. The comparison follows Fig. 3 of the manuscript. As discussed in the manuscript, this combination of data and classifier is the hardest to train the *Explainer* on.

As for previous comparisons, GCam shows accurate but very smooth attributions. RISE and EP behave similarly, by attributing the classification on the correct areas of the input image, but failing in focusing on precise image locations. iGOS++ once again shows small attributions, which in many cases lead to clear explanations but sometimes might also leave out parts where the other methods agree that they are important as well. In some cases it also includes artifacts, which make the interpretation harder. RTIS overpredicts the attributions, in particular when the objects of interest are small with respect to the input image plane. Our *Explainer* shows very clear attributions in most cases but sometimes also includes artifacts that occur as an active area in the top portion of the image. We have found that this specifically happens in images with the “person” class. Nonetheless, we can notice that the attribution masks are still precise and sharp in the object areas, suggesting that better results could probably be achieved by better hyperparameter and model selection.

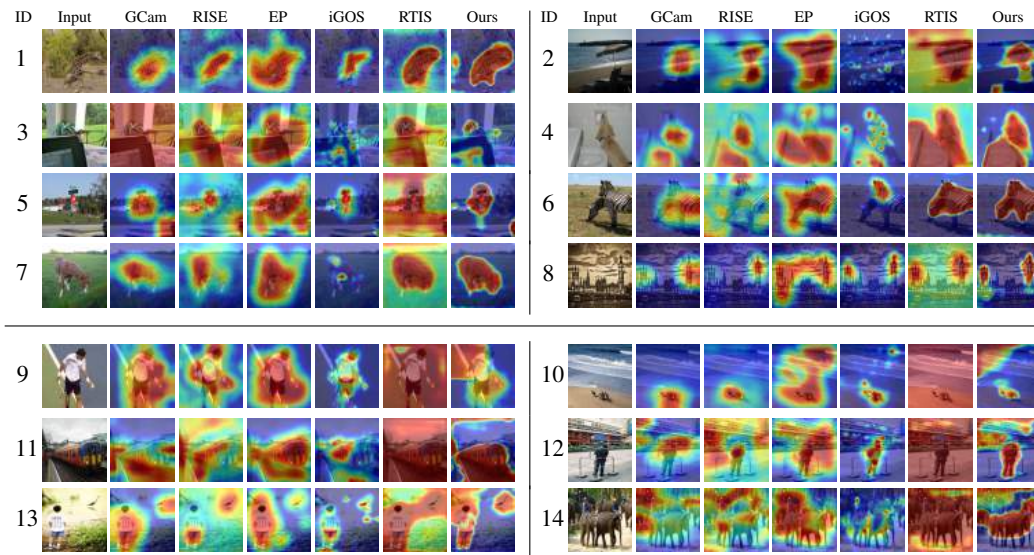


Figure 8: Comparison of attributions methods for a ResNet-50 network fine-tuned on images from the COCO-2014 dataset. Refer to Fig. 3 of the manuscript for more details.